Chinese Chemical Letters 35 (2024) 109144

Contents lists available at ScienceDirect

Chinese Chemical Letters

journal homepage: www.elsevier.com/locate/cclet

Hybrid ionic/electronic interphase enabling uniform nucleation and fast diffusion kinetics for stable lithium metal anode

Lun Li[a], Pengxia Ji[b], Meng Huang[c,*], Zixin Zhang[a], Hong Wang[a], Francis Verpoort[a], Jinlong Yang[b,*], Daping He[d,e,*]

[a] State Key Laboratory of Advanced Technology for Materials Synthesis and Processing, School of Materials Science and Engineering, Wuhan University of Technology, Wuhan 430070, China
[b] Guangdong Research Center for Interfacial Engineering of Functional Materials, College of Materials Science and Engineering, Shenzhen University, Shenzhen 518060, China
[c] Sanya Science and Education Innovation Park of Wuhan University of Technology, Sanya 572000, China
[d] Hubei Engineering Research Center of RF-Microwave Technology and Application, Wuhan University of Technology, Wuhan 430070, China
[e] State Key Laboratory of Silicate Materials for Architectures, Wuhan University of Technology, Wuhan 430070, China

ARTICLE INFO

Article history:
Received 20 August 2023
Revised 8 September 2023
Accepted 22 September 2023
Available online 29 September 2023

Keywords:
Lithium metal anode
Hybrid ionic/electronic interphase
Solid electrolyte interphase
Fast diffusion kinetics
Dendritic growth of lithium

ABSTRACT

Lithium (Li) dendrite issue, which is usually caused by inhomogeneous Li nucleation and fragile solid electrolyte interphase (SEI), impedes the further development of high-energy Li metal batteries. However, the integrated construction of a high-stable SEI layer that can regulate uniform nucleation and facilitate fast Li-ion diffusion kinetics for Li metal anode still falls short. Herein, we designed an artificial SEI with hybrid ionic/electronic interphase to regulate Li deposition by *in-situ* constructing metal Co clusters embedded in LiF matrix. The generated Co and LiF both enable fast Li-ion diffusion kinetics, meanwhile, the lithiophilic properties of Co clusters can serve as Li-ion nucleation sites, thereby contributing to uniform Li nucleation and non-dendritic growth. As a result, a dendrite-free Li deposition with a low overpotential (16.1 mV) is achieved, which enables an extended lifespan over 750 h under strict conditions. The full cells with high-mass-loading $LiFePO_4$ (11.5 mg/cm^2) as cathodes exhibit a remarkable rate capacity of 84.1 mAh/g at 5 C and an improved cycling performance with a capacity retention of 96.4% after undergoing 180 cycles.

Lithium-metal batteries (LMBs) are highly demanded in high-energy-density storage systems, owing to the ultra-high theoretical capacity (3860 mAh/g) and low reduction potential (−3.04 V *vs.* standard hydrogen electrode) of metallic Li [1,2]. However, the undesired Li dendrites are still challenging the safety issues and durability of as-built LMBs, hindering the practical implementation of LMBs [3,4]. The underlying causes are the infinite volume expansion and the violent reactivity of Li metal with electrolyte during cycling, resulting in the fracture of unstable solid electrolyte interphase (SEI) layer [5,6].

Numerous substantial solutions, such as using solid-state electrolytes [7–9], adding electrolyte additives [10,11], and constructing artificial interface layer [12,13], have been developed to build a stable and sturdy Li-electrolyte interface. Despite electrolyte component optimization and high-concentration electrolytes are proven to effectively alleviate the dendrite formation and increase the Coulombic efficiency (CE), the persistent consumption of additives or salts may aggravate the SEI structural evolution and results in unstable Li plating/stripping, leading to the decline in CE and capacity. Notably, artificial interface layer engineering, especially the *in-situ* formed LiF-rich SEI, shows great promise in accelerating Li-ion transport and stabilizing Li/electrolyte interface [14–17]. The main reasons are as follows: (1) LiF has a high ionic conductivity which ensures fast Li-ion diffusion kinetics; (2) LiF shows low Li-ion diffusion energy barriers and high surface energy, thus allowing sufficient Li-ion diffusion in a lateral manner; (3) LiF has a high mechanical strength, which is beneficial to suppressing large volume expansion and dendrite formation during repeated cycling [18,19].

It is generally accepted that uniform Li deposition involves fast Li-ion transport, strong adsorption, uniform nucleation, and controlled growth [20–22]. The first two steps of fast diffusion and strong adsorption of Li ions are prerequisite to achieve uniform nucleation and determine final growth morphology. One of the

* Corresponding authors.
E-mail addresses: 211808@whut.edu.cn (M. Huang), yangjl18@szu.edu.cn (J. Yang), hedaping@whut.edu.cn (D. He).

https://doi.org/10.1016/j.cclet.2023.109144
1001-8417/

most effective methods for constructing strong Li-ion adsorption is homogeneously coating lithiophilic seeds, such as Ag [23,24], Au [25,26], and Co [27–29] nanoparticles on copper (Cu) substrate to regulate nucleation behaviors and realize stable Li deposition. Considering the high cost of precious metals, researchers have focused on transition metallic Co and Ni nanoparticles as uniform Li nucleation sites. For example, Lou *et al.* introduced highly dispersed Ni and Co particles on the N-doped carbon fibers as nucleation sites, which enabled the uniform Li nucleation and non-dendritic growth as well as a long lifespan of LMB [28]. Yu *et al.* stabilized the Li metal anode by using Co nanoparticles and doped N atoms as active sites to regulate uniform Li nucleation and reduce the nucleation overpotential. These transition metals (*e.g.*, Co or Ni) serve as lithiophilic adsorption sites for Li nucleus landing [29]. One can expect that combining the advantages of lithiophilic nucleation sites and high-ionic conductive LiF matrix can control uniform and highly stable Li deposition.

Herein, a hybrid ionic/electronic interphase composed of Co clusters and LiF matrix is constructed by an *in-situ* electrochemical reduction of cobalt fluoride (CoF_2). Uniformly distributed Co clusters in the LiF matrix cannot only provide abundant adsorption sites for Li ions, but also prompt fast Li-ion diffusion. Additionally, the LiF matrix can also provide fast Li-ion diffusion path and strong mechanical strength to limit dendrite growth. As a result, the multi-functional artificial SEI decorated anode achieves dendrite-free Li deposition at 4 mA/cm^2, 6 mAh/cm^2. Co-LiF@Cu||Li half cells manifest an ultralow nucleation overpotential of 16.1 mV and a high CE of 98.0%. When coupled with $LiFePO_4$ (LFP) cathode with a high mass loading of 11.5 mg/cm^2, the full cell shows significantly enhanced rate performance and cycling stability. This novel anode design enables superior durability and feasibility of the high-energy-density LMBs for practical application.

We first employed density functional theory (DFT) calculations to deeply understand the function mechanism of the Co-LiF hybrid ionic/electronic interphase. The surface models of Cu (111), Co (002), and LiF (100) were considered for investigating the Li-ion adsorption due to their lowest surface energies, respectively [14,30,31]. As shown in Fig. 1a, LiF has weak affinity to Li ions with a lower adsorption energy of −0.4 eV, indicating that LiF has low lithiophilicity. While the adsorption energy of Co to Li ions (−2.9 eV) is much higher, which suggests that Co species can serve as adsorption sites to anchor Li ions. Although Cu has an adsorption energy of −2.5 eV, its uneven local electric field caused by the rough surfaces inevitably leads to randomly oriented Li nucleus [31–33], which finally evolves into dendritic morphology (Fig. 1d). Moreover, the diffusion energy barriers of Li ion on the (110), (100), and (111) facets of Li_2O are 0.65, 0.56, and 0.39 eV, respectively. By contrast, LiF has lower values of 0.36, 0.12, and 0.2 eV along the corresponding migration paths, respectively, and Co has the lowest value of 0.02 eV on the (002) crystal planes (Fig. 1b). The related Li diffusion paths are shown in Fig. 1c and Fig. S1 (Supporting information). The high adsorption energy of Co to Li ions, and fast diffusion kinetics of Li ions on both Co and LiF raise a propose that the *in-situ* constructing Co-LiF hybrid SEI can effectively suppress the dendrite formation, during which Co and LiF can disperse Li-ion flux and enable uniform diffusion within the hybrid layers, and Co species provide abundant nucleation sites for Li deposition. Thereafter, the artificial Co-LiF hybrid SEI is designed to guide homogenous Li nucleation and further growth (Fig. 1e). First, a mixed layer composed of CoF_2 was coated on the Cu foil (Fig. S2 in Supporting information). Second, the nano-size Co clusters embedded LiF matrix are generated by electrochemical reduction of CoF_2. During the Li deposition, Li ions turn into Li-ion flux with the help of LiF layers, then adsorb on the lithiophilic Co clusters, and finally are reduced to form abundant Li nucleus under small nucleation energy barriers. These fresh Li nuclei further grow in a lateral pattern guided by LiF matrix. More importantly, the hybrid Co-LiF SEI with low ion migration energy barrier favors the migration of Li ions through the Li-SEI interface, realizing dense and uniform Li deposition.

The initial CoF_2 shows a hexagonal octahedral shape with a lateral diameter of ~6 μm and a thickness of ~2 μm, showing ele-

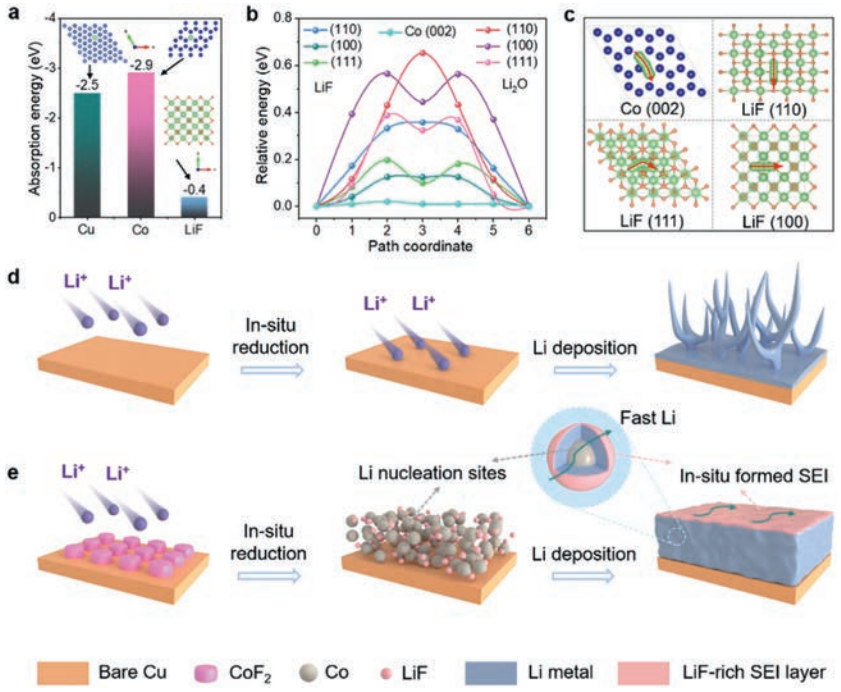

Fig. 1. Design principles of hybrid ionic/electronic interphase for stable Li metal anode. (a) Adsorption energy toward Li ion from different species. (b) Diffusion energy barriers of Li ion on different crystal planes of Co, LiF and Li_2O, respectively. (c) The corresponding diffusion pathways of Li ions for Co and LiF species. Design and functioning mechanism of (d) bare Cu foil and (e) Co-LiF@Cu electrode.

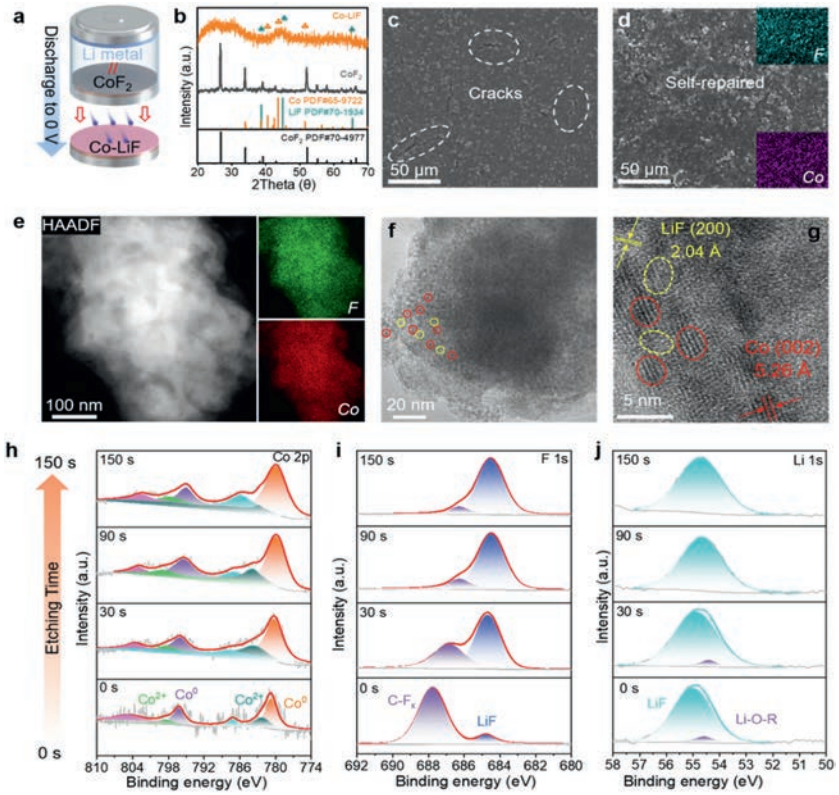

Fig. 2. Preparation and characterization of Co-LiF hybrid SEI by *in-situ* electrochemical reduction of CoF_2. (a) Synthesis route for a Co-LiF@Cu electrode. (b) XRD patterns of CoF_2 and the obtained Co-LiF hybrid layer by *in-situ* reduction. SEM images of (c) the CoF_2 electrode and (d) Co-LiF@Cu electrode. (e) TEM images and the related elemental mapping of Co-LiF nanocomposite. (f) STEM images and (g) HRTEM images of Co cluster and LiF matrix. XPS etching analysis of the Co-LiF@Cu electrode for (h) Co 2p, (i) F 1s, and (j) Li 1s after discharging to 0 V.

ment homogeneity of Co and F (Fig. S3 in Supporting information). This structure is composed of orderly stacked nanorods with diameter of ~15 nm, presenting a polycrystalline nature (Fig. S4 in Supporting information). As illustrated in Fig. 2a, coin cells were assembled using the CoF_2@Cu as working electrode and Li foil as counter electrode, and then discharged to 0 V to obtain a hybrid Co-LiF interphase on Cu. A distinct and long plateau at 1.4 V appears in the first discharge profiles (Fig. S5 in Supporting information), which can be attributed to the conversion reaction: $CoF_2 + 2Li^+ + 2e^- \rightarrow 2LiF + Co$ [15,34–36]. Fig. 2b displays the X-ray diffraction (XRD) patterns of the initial CoF_2 and its reduction products of Co-LiF hybrid layer. CoF_2 exhibits clear and sharp XRD diffraction peaks (PDF#70-4977), suggesting its high purity and high crystallinity. After reduction, the peaks of CoF_2 disappear and new peaks indexed to hexagonal Co (PDF#65-9722) and cubic LiF (PDF#70-1934) are observed, confirming the successful construction of metallic Co and LiF hybrid composite. The wide and dispersed XRD peaks indicate the nanocrystalline nature of the Co and LiF products [35]. Scanning electron microscopy (SEM) images of CoF_2@Cu electrode and its surface after electrochemical reduction are presented in Figs. 2c and d and Fig. S6 (Supporting information). It is noticed that numerous cracks were developed in the CoF_2@Cu electrodes, while they were self-repaired after discharged to 0 V, which can be attributed to the redispersion of Co and LiF during the phase change process [15,35]. F and Co elements are homogeneously dispersed through the Co-LiF layer (Fig. 2d inset and Fig. S6b). Transmission electron microscopy (TEM) and high-resolution TEM (HR-TEM) were further applied to analyze the microstructure of Co and LiF. The homogeneous distributed Co and F elements (Fig. 2e) indicate the nanoscale mixing of LiF and Co. Figs. 2f and g show that Co and LiF exist in the form of clusters, and Co (red circle) is uniformly embedded in the LiF (yellow circle) matrix. The Co and LiF nanoparticles with a diameter of ~3 nm have lattice spacings of 5.26 and 2.04 Å, corresponding to (002) crystal plane of hexagonal Co and (200) of cubic LiF, respectively.

To further clarify the chemical composition of the SEI in depth, we proceeded X-ray photoelectron spectroscopy (XPS) with Ar^+ sputter etching (Figs. 2h–j). Compared with the XPS results of the initial CoF_2 (Fig. S7 in Supporting information), the artificial SEI shows two major peaks at lower energy of 780.7 and 796.2 eV on the upper surface, which are assigned to Co 2p of metallic Co (Fig. 2h) [35,37]. Slight doublet peaks at 782.1 and 798.4 eV belong to Co^{2+} $2p_{3/2}$ and Co^{2+} $2p_{1/2}$ [38,39], respectively, which may originate from the partially oxidized surface of the Co clusters. After etching for 30 s, the obviously increased peak intensity and area of metallic Co confirm that Co^0 dominates inside the SEI bulk. The high-resolution F 1s and Li 1s XPS results confirm the presence of LiF at 684.8 (Fig. 2i) and 55.0 eV (Fig. 2j) on the upper surface of the electrode, respectively [40–43]. After etching over 30 s, the LiF content significantly increase, whereas the C-F_x content is reduced, which indicates that the C-F_x is derived from the residual electrolyte [40]. However, an extremely weak signal of LiF emerges on the F 1s spectrum for bare Cu after reduction, implying that the content of LiF produced by the electrolyte decomposition is negligible (Fig. S8 in Supporting information). Therefore, the expected Co-LiF hybrid ionic/electronic interphase is successfully constructed.

To elucidate the stability of the hybrid Co-LiF interphase after Li plating, the composition of Li-deposited Co-LiF@Cu electrode was analyzed at different depth by Ar^+ sputter etching. The disappearance of Co^{2+} can be attributed to the reduction by the deposited metallic Li. For metallic Co, the absence of signal for at 0 s and

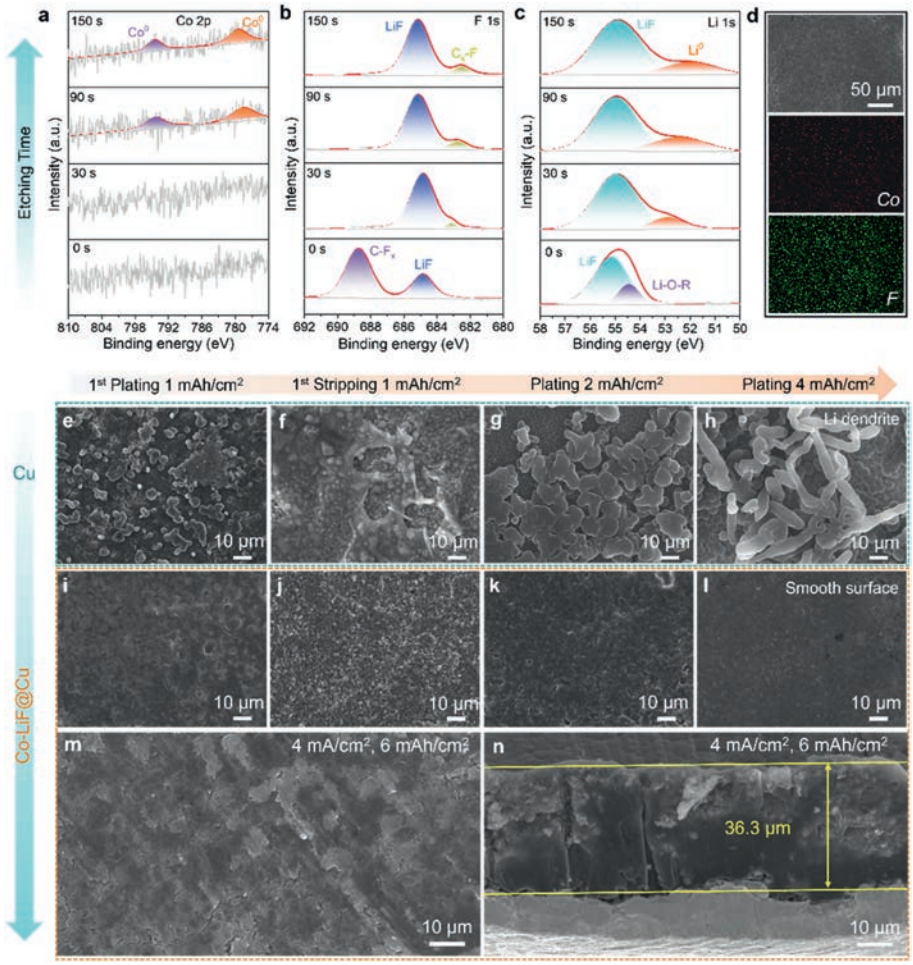

Fig. 3. Characterization of the Li-deposited Co-LiF@Cu electrode. (a) Co 2p, (b) F 1s, and (c) Li 1s XPS etching analysis of the Co-LiF@Cu electrode after depositing Li with 1 mAh/cm^2. (d) The corresponding element mapping. SEM images of (e-h) bare Cu and (i-l) Co-LiF@Cu electrode after 1st Li plating/stripping at 1 mA/cm^2, 1 mAh/cm^2 and further depositing Li with increased capacity to 2 and 4 mAh/cm^2. (m) Top-view and (n) cross-sectional images of Co-LiF@Cu electrode with plated Li at 4 mA/cm^2, 6 mAh/cm^2.

30 s and the appearance at 90 s (778.4 and 794.2 eV) and 150 s (Fig. 3a) indicates that the Co clusters were covered by the deposited Li metal on the surface, suggesting that the Co preferentially serves as initial nucleation site. Noted that LiF XPS peaks are clearly identified on the upper surface (Fig. 3b), and the contents of the LiF change little after etching from 30 s to 150 s, which suggests that the components of the inner LiF are stable and uniform. Beside, a weak peak at 683.1 eV emerges after etching for 30 s, indicating the existence of ionic fluorine atom in C_x-F [44]. The special formation of C_x-F component may occur in the presence of initially plated Li [45]. For Li 1s pattern, two peaks at 54.4 and 55.1 eV are assigned to Li-O-R and LiF, respectively, however, XPS peak of metallic Li is not observed on the outermost surface. With etching time increasing over 30 s, independent Li^0 peak located at 52.9 eV is observed, indicating metallic Li [46] is deposited underneath the SEI layer (Fig. 3c). The top-view EDS images also show the homogenous F and slight absence of Co distribution on the surface after Li deposition (Fig. 3d), implying the coverage of metallic Li on the Co surface and the conformal protection of LiF on deposited Li.

To verify the optimized Li plating/stripping behaviors regulated by the lithiophilic Co sites and LiF matrix, we assembled asymmetric cells to reveal the morphology evolution for Li deposition at different deposition capacity. 1.0 mol/L LiTFSI in a liquid mixture of 1,2-dimethoxyethane and 1,3-dioxolane (1:1, v/v) with 1 wt% $LiNO_3$ additive was used as the electrolyte. At 1 mA/cm^2, 1 mAh/cm^2, plenty irregular Li particles appear on the Cu surface (Fig. 3e and Fig. S9a in Supporting information), and a large amount of 'dead' Li and cavities are produced after stripping (Fig. 3f), leading to a disordered and rough morphology. With the capacity increased to 2 and 4 mAh/cm^2, Li particles gradually grow into large Li lumps and finally evolved into randomly oriented Li dendrites (Figs. 3g and h), showing high risk to penetrating the separator. In contrast, the uniform Li deposition is guaranteed for the Co-LiF@Cu electrode. As presented in Fig. S10a (Supporting information), when the Li deposition capacity is 1 mAh/cm^2, some pancake-like Li metal with different sizes covered on the surface Co-LiF@Cu electrode. The magnified SEM suggests that the surface of pancake-like Li is relatively flat and smooth (Fig. 3i). Cross-sectional SEM images show a dense Li filled Co-LiF layer which is tightly attached to the Cu substrate (Fig. S9b in Supporting information). As shown in Figs. S9c and d (Supporting information), a large area of Li sheets deposit underneath and in the inner pores of Co-LiF layer. The elemental mapping results show the absence of Co and uniform distribution of F (Fig. S9e and f in Supporting information), indicating that Co are completely covered by the plated Li, while LiF layer acts as a protective layer. After 1st stripping (Fig. 3j), the Co-LiF@Cu electrode can be restored to the original surface shown in Fig. 2d, demonstrating a good reversibility of Li plating/stripping. As the Li amount increases to 2 mAh/cm^2, pancaked-like and smooth-faced Li gradually connected (Fig. 3k and Fig. S10b in Supporting infor-

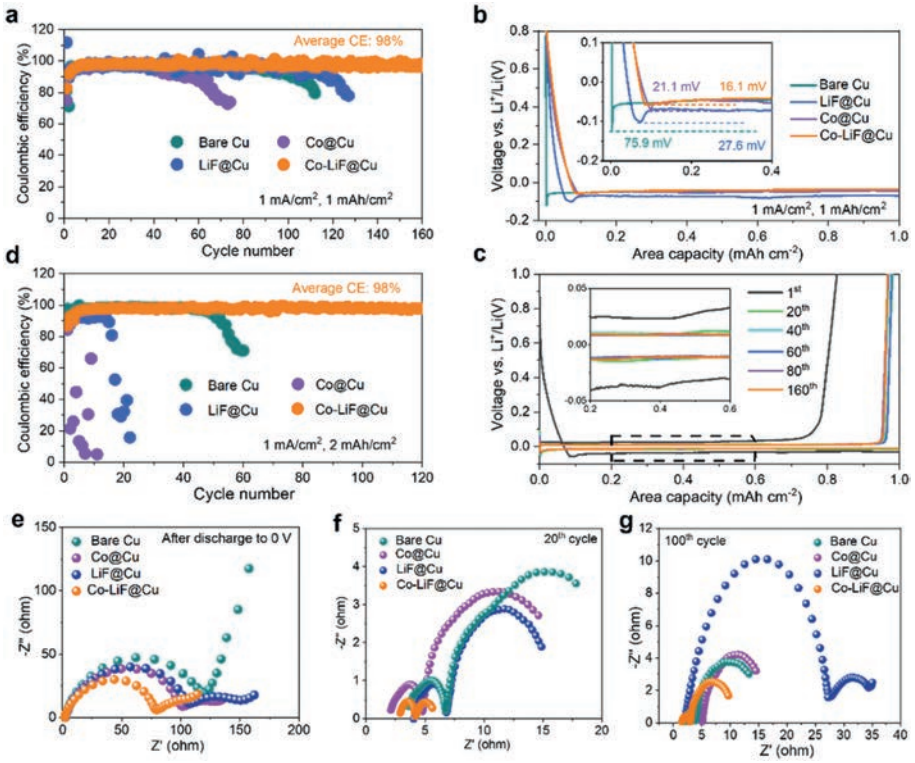

Fig. 4. Electrochemical performance of half cells with different substrates. (a) CEs of bare Cu, LiF@Cu, Co@Cu, and Co-LiF@Cu at 1 mA/cm^2, 1 mAh/cm^2. (b) Nucleation overpotentials of different anodes at 1 mA/cm^2, 1 mAh/cm^2. (c) The corresponding Li plating/stripping curves after different cycles. (d) CEs of different anodes at 1 mA/cm^2, 2 mAh/cm^2. Nyquist plot of half cells based on different substrates after (e) 1st discharging to 0 V, (f) 20 cycles, and (g) 100 cycles at 1 mA/cm^2, 1 mAh/cm^2, respectively.

mation), and the surface gets more compact and smoother when the plating capacity reaches to 4 mAh/cm^2 (Fig. 3l). Furthermore, when the current density and deposition capacity are increased to 4 mA/cm^2 and 6 mAh/cm^2, the Li deposited Co-LiF@Cu electrode is seamlessly contacted, leading to a flat and dendrite-free plating surface (Fig. 3m). In addition, cross-sectional SEM image clearly shows a dense deposition structure with a thickness of ~36.3 μm, corresponding to a ~26.3 μm thick Li deposition on the electrode surface (Fig. 3n and Fig. S6b). The dendrite-free and reversible Li plating/stripping on Co-LiF@Cu indicates the validity of abundant nucleation sites, fast diffusion kinetics, and effective protection endowed by Co-LiF ionic/electronic interphase.

To further evaluate the sustainability and practicality of Li plating/stripping, four types of asymmetrical cells using different electrodes were assembled to test their CEs. The Co-LiF@Cu electrode exhibits superior cyclability and longer cycling life compared with Co@Cu, LiF@Cu, and bare Cu electrodes (Fig. 4a). Specifically, the Co-LiF@Cu electrode manifests a more stable CE around 98.0% over 160 cycles under 1 mA/cm^2, 1 mAh/cm^2. By contrast, the CEs of Co@Cu, LiF@Cu, and bare Cu electrodes decrease to 73.9%, 78.0% and 79.6% after 74, 127, and 112 cycles, respectively. Fig. 4b shows that the Co-LiF@Cu electrode has the lowest nucleation overpotential of 16.1 mV, which is much lower than that of bare Cu (75.9 mV), Co@Cu (21.1 mV), and LiF@Cu (27.6 mV). The ultralow nucleation overpotential of Co-LiF@Cu verifies the improved nucleation thermodynamics and fast Li-ion diffusion kinetics driven by the synergistic effect of the lithiophilic sites and fast Li-ion diffusion. Correspondingly, the plating/striping plateaus of Co-LiF@Cu at different cycles are steady and overlapped (Fig. 4c), indicating a highly stable and reversible Li plating/stripping behavior. Consequently, when the plating capacity increases to 2 mAh/cm^2, the CE of Co-LiF@Cu can still be held at 98.0% after 120 cycles (Fig. 4d), which is greatly enhanced compared with other three electrodes. Even the current and deposition capacity is increased to 2 mA/cm^2 and 4 mAh/cm^2, the Co-LiF@Cu still enables a uniform Li plating/stripping (Fig. S11 in Supporting information). The unstable CEs and Li deposition behavior of the mixed electrode of acetylene black and PVDF (Fig. S12 in Supporting information) again confirms the critical and positive effect of Co-LiF hybrid ionic/electronic interphase on Li plating/stripping. Figs. 4e–g show the electrochemical impedance spectroscopy (EIS) of different electrodes. All the fresh electrodes have single semicircle (Fig. S13 in Supporting information), which corresponds to the charge transfer resistance (R_{ct}) between the original electrode and electrolyte [19]. After discharging to 0 V, new semicircle emerges in the Nyquist plot of Co@Cu, LiF@Cu, and Co-LiF@Cu electrodes (Fig. 4e), suggesting a new interfacial resistance (R_{sei}) induced by the *in-situ* formed SEI. As expected, the Co-LiF@Cu electrode shows the lowest R_{sei} in high frequency range, indicates that the formed Co and LiF species enable better electrolyte wettability and fast Li-ion diffusion. After Li plating/stripping 20 and 100 cycles, Co-LiF@Cu electrode not only exhibits the smallest R_{sei} for Li-ion migration, but also demonstrates the lowest R_{ct} between the artificial SEI and electrolyte (Figs. 4f and g), validating the fast Li-ion diffusion kinetics and confirming the high structural stability of Li@Co-LiF@Cu anode. The Tafel curves and activation energy of pristine Li and Li@Co-LiF@Cu symmetric cells are shown in Figs. S14a and b (Supporting information). Compared with pristine Li anode, Li@Co-LiF@Cu anode illustrates a higher exchange current density and a lower E_a, demonstrating that Li ion diffusion through the SEI is accelerated due to the introduction of the introduction of Co-LiF hybrid interphase. Therefore, this hybrid ionic/electronic interphase can effectively promote the adsorption/diffusion of Li ions, thereby improving the cyclability of Li metal anodes.

Furthermore, we investigated the superiority of the Co-LiF bifunctional modification strategy for Li metal anode by using sym-

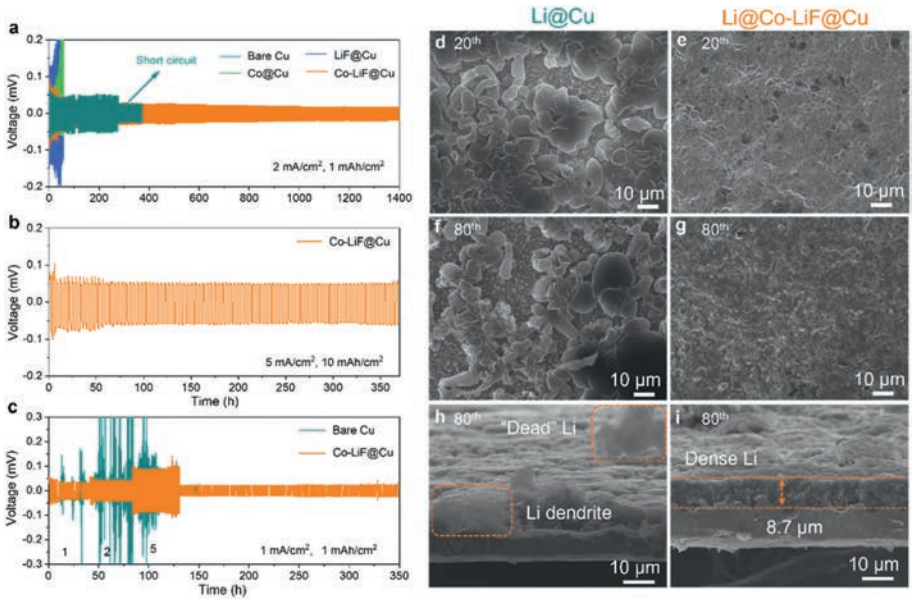

Fig. 5. Cycling stability of composited Li metal anodes in symmetrical cells. (a) The voltage profiles of Li@Cu, Li@LiF@Cu, Li@Co@Cu, and Li@Co-LiF@Cu anodes in symmetrical cells at 2 mA/cm^2, 1 mAh/cm^2. (b) The voltage profiles of Li@Co-LiF@Cu anode in symmetrical cell at 5 mA/cm^2, 10 mAh/cm^2. (c) The voltage profiles of Li@Co-LiF@Cu and Li@Cu anodes in symmetrical cells at 1, 2, 5 mA/cm^2 for 1 mAh/cm^2. Top-view and cross-sectional SEM images of (d, f, h) Li@Cu and (e, g, i) Li@Co-LiF@Cu anodes after 20 and 80 cycles, respectively.

metrical cells. Before assembly, metallic Li with an area capacity of 3 mAh/cm^2 was deposited on bare Cu, Co@Cu, LiF@Cu, and Co-LiF@Cu. As illustrated in Fig. 5a, the Li@Cu cell suffers from a dendritic short circuit at 2 mA/cm^2, 1 mAh/cm^2 after cycling for 276 h. The voltage polarizations of Li@Co@Cu and Li@LiF@Cu symmetrical cells drastically increase to exceeding 300 mV within 60 h, which suggests that the fragile/unstable SEI structure or highly porous Li dendrite can cause the severe side reaction, leading to the depletion of electrolyte and early death of the Li metal anode [47,48]. By comparison, the Li@Co-LiF@Cu symmetrical cell shows a remarkably long cycle life and a steady voltage hysteresis about 37 mV for more than 1400 h. As the current and capacity increase to 5 mA/cm^2 and 10 mAh/cm^2, the symmetric Li@Co-LiF@Cu cell still holds excellent stability for over 370 h with a moderate rise in voltage hysteresis (Fig. 5b). The rate performance shows that the symmetric cell with Li@Cu exhibits a severe voltage fluctuation and suffers from electrode failure after cycling for 13 h (Fig. 5c). With regard to Li@Co-LiF@Cu symmetrical cell, the voltage hysteresis steadily increases from 35 mV to 41 and 88 mV with the current densities varying from 1 mA/cm^2 to 2 and 5 mA/cm^2. Particularly, this cell can stably cycle with an overpotential of 23 mV after suffering from high-rate Li plating/stripping, indicating a good rate capability and reversibility. Such superior electrochemical properties can be ascribed to the unobstructed electronic/ionic transport paths, which can induce uniform and stable Li plating/stripping even at high current densities and capacities.

The Li deposition morphologies after 20th and 80th plating at 1 mA/cm^2, 1 mAh/cm^2 are shown in Figs. 5d–i. The Li@Cu exhibits a rough surface with randomly oriented Li chunks, numerous Li dendrites and 'dead' Li with the increase of plating numbers (Figs. 5d, f and h), indicating uneven Li deposition and uncontrolled dendrites growth. This undesired Li deposition can lead to the increase of voltage polarization and resistance. Needle-like dendrites inevitably cause the short circuit of batteries, thus threatening battery safety. After decorated with Co clusters and LiF matrix, the Li@Co-LiF@Cu exhibits a smooth and compact Li deposition without any Li dendrites and blocks after cycling for 20 and 80 times (Figs. 5e and g). At the enlarged view, it can be clearly observed that deposited Li fills the pores in the of Co-LiF/Cu electrode and develops in a lateral growth pattern, thus forming an integrated and flat surface (Fig. S15 in Supporting information). The thickness of the deposited layer at 80th cycle is 8.7 μm (Fig. 5i), which is in accordance with the initial plating morphology (Fig. S9b in Supporting information). Even after 80th plating, clear LiF signal and absence of metal Li are detected, which suggests that LiF stably covers on the surface of plated Li (Fig. S16 in Supporting information). The robust LiF layer as a physical protective barrier can avoid severe side reaction between electrolyte and highly reactive Li, enabling highly reversible Li plating/stripping behavior. As a result, the Li@Co-LiF@Cu symmetrical cell can achieve an extended cycling lifespan.

To further assess the application possibility of Li@Co-LiF@Cu anode in practical LMBs, we assembled full cells paired with high-mass-loading LFP cathode (11.5 mg/cm^2, N/P ratio is 3:1) (Fig. 6a). After charging to 4 V, the LFP||Li@Cu pouch cell can stably power a light emitting diode (LED) without attenuation of brightness (Fig. 6b), demonstrating the practicality and durability of the Li@Co-LiF@Cu anode. Fig. 6c exhibits the discharge/charge curves of LFP||Li@Co-LiF@Cu full cell at different rates. Compared with LFP||Li@Cu (Fig. S17 in Supporting information), the LFP||Li@Co-LiF@Cu full cell demonstrates a stable voltage plateaus and enhanced rate capability. The specific capacities of LFP||Li@Co-LiF@Cu full cell are 157.8, 146.3, 132.8, 113.2, and 84.1 mAh/g at 0.2, 0.5, 1, 2, and 5 C, respectively (Fig. 6d). As the current density turns back to 0.2 C, the specific capacity returns to 153.5 mAh/g, demonstrating an excellent stability of the Li@Co-LiF@Cu anode in full cells. However, full cell of LFP||Li@Cu shows a distinctly lower capacity starting from 1 C. When tested at 5 C, the discharge capacity deteriorates to almost zero, indicating the high-rate failure of LFP||Li@Cu battery. Furthermore, the LFP||Li@Co-LiF@Cu full cell shows much smaller polarization voltage at all current densities (Fig. 6e), and when the current density is back to 0.2 C, the polarization voltage (52.1 mV) almost recovers to the initial levels (51.7 mV). The full cells with Li@Co-LiF@Cu anodes demonstrate better cycling stability than that with Li@Cu anodes (Fig. 6f). As illustrated in Fig. 6g, LFP||Li@Co-LiF@Cu manifests a higher initial

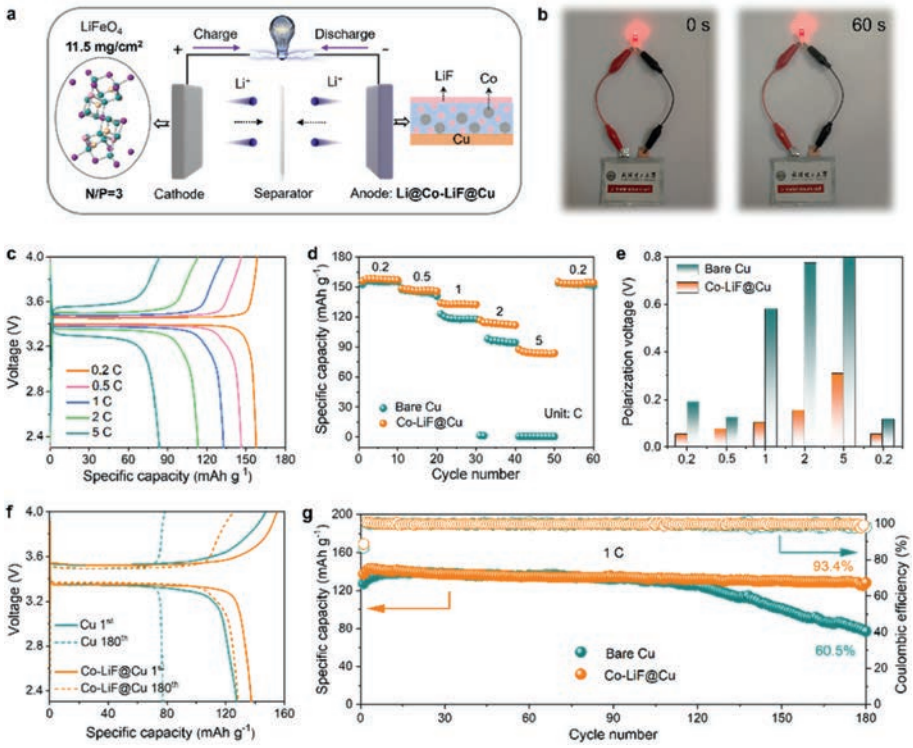

Fig. 6. Electrochemical performance of full cells. (a) Schematic illustration of the LFP||Li@Co-LiF@Cu full cell. (b) The LED lightened by the LFP||Li@Co-LiF@Cu pouch cell. (c) Discharge/charge profiles of the LFP||Li@Co-LiF@Cu full cell at different current densities. (d) Rate capability and (e) the polarization voltage of LFP||Li@Cu and LFP||Li@Co-LiF@Cu full cells. (f) Discharge/charge profiles of LFP||Li@Cu and LFP||Li@Co-LiF@Cu full cells at different cycles. (g) Long-term cycling stability of the two types of full cells.

capacity of 137.4 mAh/g, 93.4% of which is maintained at 180th cycle. Comparatively, the capacity of LFP||Li@Cu full cell severely decays from 127.5 mAh/g to 77.2 mAh/g after 180 cycles, with a much lower capacity retention of 60.5%. Beside, the initial CE of LFP||Li@Co-LiF@Cu battery (88.7%) is higher than that of LFP||Li@Cu battery (86.7%), and maintains stably at ~99.2% during the cycling, while serious CE fluctuation appears after 130 cycles for LFP||Li@Cu full cell. The better rate capability, longer cycling life, and lower polarization of LFP||Li@Co-LiF@Cu full cells are benefited from the fast Li-ion diffusion kinetics, preferred deposition thermodynamics, and protective function enabled by Co-LiF interphase layer. These advanced performances evident the superiority of Li@Co-LiF@Cu anode and confirm its feasibility for practical Li batteries.

In summary, a novel Co-LiF hybrid ionic/electronic interphase of on Cu substrate for Li metal anode has been successfully designed and fabricated. The lithiophilic Co seeds exhibit strong absorption to Li ions, thus can effectively guide uniform Li nucleation. Meanwhile, both the Co clusters and LiF matrix enable fast Li-ion transport effect, providing abundant transport paths to boost Li diffusion kinetics and stabilizing the Li/electrolyte interface. With this strategy, the Co-Li@Cu can achieve a dendrite-free Li deposition even under high current and high plating capacity. Consequently, Co-Li@Cu||Li half cells could stably undergo plating/stripping with a high CE of ~98.0%. The symmetric cells achieve a long-term cycling life beyond 1400 h and 370 h under 2 mA/cm^2, 1 mAh/cm^2 and 5 mA/cm^2, 10 mAh/cm^2, respectively. When paired with LFP cathodes with mass loading of 11.5 mg/cm^2, the full cells with a N/P ratio of 3 exhibit a high rate performance (84.1 mAh/g at 5 C) and can be cycled for 180 cycles with a high capacity retention of 93.4%. The rationally designed Co-LiF hybrid ionic/electronic structure with lithiophilic nucleation sites, high ionic conductivity and protective function shows great promise for constructing high-performance LMBs.

Declaration of competing interest

The authors declare that they have no conflict of interest.

Acknowledgments

This work was financially supported by the National Natural Science Foundation of China (Nos. 22279097, 52172217), Natural Science Foundation of Guangdong Province (No. 2021A1515010144), and Shenzhen Science and Technology Program (No. JCYJ20210324120400002).

Supplementary materials

Supplementary material associated with this article can be found, in the online version, at doi:10.1016/j.cclet.2023.109144.

References

[1] Y. Liu, X. Tao, Y. Wang, et al., Science 375 (2022) 739–745.
[2] Z. Wu, C. Wang, Z. Hui, et al., Nat. Energy 8 (2023) 340–350.
[3] Y. Xiang, M. Tao, G. Zhong, et al., Sci. Adv. 7 (2021) eabj3423.
[4] Y. Zhang, T.T. Zuo, J. Popovic, et al., Mater. Today 33 (2020) 56–74.
[5] D. Lin, Y. Liu, Y. Cui, Nat. Nanotechnol. 12 (2017) 194–206.
[6] R. Xu, X.B. Cheng, C. Yan, et al., Matter 1 (2019) 317–344.
[7] S. Zhang, G. Yang, Z. Liu, et al., Nano Lett. 21 (2021) 3310–3317.
[8] Y. Liu, D. Lin, Y. Jin, et al., Sci. Adv. 3 (2017) eaao0713.
[9] S. Ye, L. Wang, F. Liu, et al., Adv. Energy Mater. 10 (2020) 2002647.
[10] Y. Wang, Z. Wang, L. Zhao, et al., Adv. Mater. 33 (2021) 2008133.
[11] X. Zhang, X. Cheng, X. Chen, C. Yan, Q. Zhang, Adv. Funct. Mater. 27 (2017) 1605989.
[12] Q.J. Ke, Q.S. Xu, X.J. Lai, et al., Chin. Chem. Lett. 34 (2023) 107602.
[13] J.C. Cui, T.G. Zhan, K.D. Zhang, D. Chen, Chin. Chem. Lett. 28 (2017) 2171–2179.
[14] A. Hu, W. Chen, X. Du, et al., Energy Environ. Sci. 14 (2021) 4115–4124.
[15] Z. Peng, N. Zhao, Z. Zhang, et al., Nano Energy 39 (2017) 662–672.
[16] H. Yuan, J. Nai, H. Tian, et al., Sci. Adv. 6 (2020) eaaz3112.
[17] Q. Zhang, X. Zhang, J. Wan, et al., Nat. Energy 8 (2023) 725–735.
[18] M. He, R. Guo, G.M. Hobold, H. Gao, B.M. Gallant, Proc. Natl. Acad. Sci. U. S. A. 117 (2020) 73–79.

[19] R. Pathak, K. Chen, A. Gurung, et al., Nat. Commun. 11 (2020) 93.
[20] P. Zou, Y. Sui, H. Zhan, et al., Chem. Rev. 121 (2021) 5986–6056.
[21] Q. He, Z. Li, M. Wu, et al., Adv. Mater. 35 (2023) 2302418.
[22] X. Chen, B.C. Zhao, C. Yan, Q. Zhang, Adv. Mater. 33 (2021) 2004128.
[23] Z.T. Wondimkun, W.A. Tegegne, J. Shi-Kai, et al., Energy Storage Mater. 35 (2021) 334–344.
[24] Z. Hou, Y. Yu, W. Wang, et al., ACS Appl. Mater. Interfaces 11 (2019) 8148–8154.
[25] T. Yang, L. Li, F. Wu, R. Chen, Adv. Funct. Mater. 30 (2020) 2002013.
[26] J. Jiang, X. Hu, S. Lu, et al., Energy Storage Mater. 54 (2023) 885–894.
[27] T. Wang, X. Liu, X. Zhao, et al., Adv. Funct. Mater. 30 (2020) 2000786.
[28] C. Chen, J. Guan, N.W. Li, et al., Adv. Mater. 33 (2021) 2100608.
[29] T. Zhou, J. Shen, Z. Wang, et al., Adv. Funct. Mater. 30 (2020) 1909159.
[30] J. Zheng, Z. Ju, B. Zhang, et al., J. Mater. Chem. A 9 (2021) 10251–10259.
[31] Y. Fang, S.L. Zhang, Z.P. Wu, D. Luan, X. Lou, Sci. Adv. 7 (2021) eabg3626.
[32] R. He, Y. Wang, C. Zhang, et al., Adv. Energy Mater. 13 (2023) 2204075.
[33] L. Li, H. Fu, J. Yang, et al., J. Mater. Chem. A 10 (2022) 11659–11666.
[34] D.H. Lee, K.J. Carroll, S. Calvin, S. Jin, Y.S. Meng, Electrochim. Acta 59 (2012) 213–221.
[35] Y. Sun, H.W. Lee, G. Zheng, et al., Nano Lett. 16 (2016) 1497–1501.
[36] Z. Gong, C. Lian, P. Wang, et al., Energy Environ. Mater. 5 (2022) 1270.
[37] R. Wang, J. Yang, X. Chen, et al., Adv. Energy Mater. 10 (2020) 1903550.
[38] L. Li, W. Chen, W. Luo, et al., Energy Technol. 7 (2019) 1801160.
[39] W. Hu, H. Fu, L. Chen, et al., Chem. Eng. J. 451 (2023) 138613.
[40] C. Cui, C. Yang, N. Eidson, et al., Adv. Mater. 32 (2020) 1906427.
[41] H. Su, H.K. Zhang, Z.F. Chen, et al., Chin. Chem. Lett. 34 (2023) 108640.
[42] K. Yang, L. Li, Y.B. Xiao, et al., Chin. Chem. Lett. (2023), doi:10.1016/j.cclet.2023.108451.
[43] S. Tan, Y. Jiang, S. Ni, et al., Natl. Sci. Rev. 9 (2022) nwac183.
[44] Y. Matsuo, T. Nakajima, Chem 621 (1995) 1943–1950.
[45] M. Wang, Z. Peng, W. Luo, et al., Adv. Energy Mater. 9 (2019) 1802912.
[46] D. Lin, Y. Liu, W. Chen, et al., Nano Lett. 17 (2017) 3731–3737.
[47] J. Wu, Z. Rao, X. Liu, et al., Adv. Mater. 33 (2021) 2007428.
[48] R. Pathak, K. Chen, A. Gurung, et al., Adv. Energy Mater. 9 (2019) 1901486.